

Pure real energy spectrum and exact anomalous mobility edges in a non-Hermitian flat band geometry

Zhanpeng Lu(陆展鹏), Hui Liu(刘辉), Yan Gu(古燕), and Zhihao Xu(徐志浩)
Citation: Chin. Phys. B, 2026, 35 (**7**): 077101. DOI: 10.1088/1674-1056/ae1efd
http://cpb.iphy.ac.cn; http://iopscience.iop.org/cpb

What follows is a list of articles you may be interested in

Grassmann corner transfer-matrix renormalization group approach to one-dimensional fermionic models

Jian-Gang Kong(孔建刚) and Zhi-Yuan Xie(谢志远)
Chin. Phys. B, 2026, 35 (**6**): 067101. DOI: 10.1088/1674-1056/ae56e3

Non-Hermitian birefringent Dirac fermions driven by electromagnetic fields

Kai Liu(刘恺), Wan-Zi Sun(孙万梓), Cheng-Xi Li(李成蹊), and Wu-Ming Liu(刘伍明)
Chin. Phys. B, 2025, 34 (**7**): 077104. DOI: 10.1088/1674-1056/adcaa1

Phase induced localization transition

Tong Liu(刘通), Xingbo Wei(魏兴波), and Youguo Wang(王友国)
Chin. Phys. B, 2024, 33 (**10**): 107103. DOI: 10.1088/1674-1056/ad6a0b

Mobility edges generated by the non-Hermitian flatband lattice

Tong Liu(刘通) and Shujie Cheng(成书杰)
Chin. Phys. B, 2023, 32 (**2**): 027102. DOI: 10.1088/1674-1056/ac6581

Non-Hermitian Kitaev chain with complex periodic and quasiperiodic potentials

Xiang-Ping Jiang(蒋相平), Yi Qiao(乔艺), and Junpeng Cao(曹俊鹏)
Chin. Phys. B, 2021, 30 (**7**): 077101. DOI: 10.1088/1674-1056/abfa08

Pure real energy spectrum and exact anomalous mobility edges in a non-Hermitian flat band geometry

Zhanpeng Lu(陆展鹏)[1], Hui Liu(刘辉)[2,†], Yan Gu(古燕)[3,‡], and Zhihao Xu(徐志浩)[2,4,§]

[1] *Department of Physics, XinZhou Normal University, Xinzhou* 034000, *China*
[2] *Institute of Theoretical Physics and State Key Laboratory of Quantum Optics Technologies and Devices, Shanxi University, Taiyuan* 030006, *China*
[3] *Shanxi Vocational University of Engineering Science and Technology, Jinzhong* 030619, *China*
[4] *Collaborative Innovation Center of Extreme Optics, Shanxi University, Taiyuan* 030006, *China*

(Received 20 August 2025; revised manuscript received 7 November 2025; accepted manuscript online 13 November 2025)

The interplay between quasi-periodicity and non-Hermiticity can give rise to rich localization phenomena. In this work, we investigate the localization transition in a one-dimensional nonreciprocal cross-stitch flat band lattice with diagonal quasi-periodic mosaic modulation, which incorporates both constant and quasi-periodic potentials. In general, nonreciprocity induces the skin effect in non-Hermitian systems through nonreciprocal transitions. However, in this work, we find that in a non-reciprocal flat band lattice, when the constant potential is zero, the skin effect does not exist in the system, and the energy spectrum remains purely real and well-defined. In the presence of a non-zero constant potential, we derive analytical solutions for a class of anomalous mobility edges (AMEs) under periodic boundary conditions (PBCs), revealing the systems localization and critical properties. Through analytic results, we demonstrate that the system is fundamentally equivalent to a generalized non-Hermitian Aubry–André (AA) model. Importantly, this equivalence implies the existence of a transition from a critical phase to a localized phase, as predicted by the non-Hermitian AA model. However, our analysis reveals that the transition point from the critical phase to the localized phase is energy-dependent, which fundamentally accounts for the emergence of AMEs. Furthermore, we design a classical electrical circuit to experimentally realize our system. This work provides new insights into localization transitions in non-Hermitian flat band systems.

Keywords: non-Hermiticity, localization transition, quasi-periodic potentials

PACS: 71.10.Fd, 71.23.An, 61.44.Br

DOI: 10.1088/1674-1056/ae1efd **CSTR:** 32038.14.CPB.ae1efd

1. Introduction

Anderson localization is one of the most prominent phenomena in disordered systems and has been experimentally validated across various platforms.[1–7] According to the single-parameter scaling theory, even an infinitesimal amount of disorder leads to the localization of all states in systems with dimensions $D \leq 2$.[8] However, this scaling theory does not extend to quasi-periodic systems. A prime example of such systems is the one-dimensional Aubry–André (AA) model,[9,10] which exhibits a transition of all eigenstates from extended to localized.[11] Quasi-periodic systems, moreover, host a variety of exotic localization transitions that are absent in random disorder systems, such as reentrant localization transitions[12–22] and cascades of delocalization transitions.[23–26] Recently, important progress in quasi-periodic systems is anomalous mobility edges (AMEs),[27,28] separating localized from critical states.[29–40] In previous studies, quasi-periodic systems typically feature energy boundaries that distinguish between extended and localized states, known as mobility edges.[41–53] The discovery of AMEs offers a fresh perspective on localization phenomena.

On the other hand, flat band lattices are garnering growing attention in the field of condensed matter physics. Flat band lattices are a class of translation-invariant systems, which contain at least one momentum-independent energy band.[54,55] Since the motion of electrons is frozen in flat band lattices, weak interactions can play a dominant role in quantum phase transitions. Consequently, flat band systems are often considered as ideal platforms to achieve exotic correlated phases or strongly correlated physics, such as the fractional quantum Hall effect.[56] Due to the macroscopic degeneracy, quasi-periodicity perturbed flat band lattices exhibit interesting localization phenomena, such as various types of localization transitions between extended states, localized states, and critical states.[57–59]

In recent years, non-Hermitian systems have attracted significant attention due to their unique properties. By introducing non-Hermitian terms into the Hamiltonian, these systems can effectively model open quantum systems. Such terms fundamentally alter the system's behavior, leading to phenomena absent in Hermitian systems, such as exceptional points,[60,61] the non-Hermitian skin effect,[62,63] and more. Additionally,

†Corresponding author. E-mail: liuhui99@sxu.edu.cn
‡Corresponding author. E-mail: guyan@sxgkd.edu.cn
§Corresponding author. E-mail: xuzhihao@sxu.edu.cn

© 2026 Chinese Physical Society and IOP Publishing Ltd. All rights, including for text and data mining, AI training, and similar technologies, are reserved.

the energy spectrum in non-Hermitian systems is often complex, enabling a richer variety of band structures in the two-dimensional complex energy plane, including point gaps and line gaps.[64–67] The interplay between non-Hermiticity and quasi-periodicity has provided new insights into localization properties, with notable findings such as the correspondence between the Anderson transition point and topological transition points.[68] However, while there has been research on AMEs, flat-band lattices, and non-Hermitian systems individually, studies exploring the interplay among these aspects remain scarce. Consequently, this area remains largely uncharted, offering significant opportunities for further investigation.

In this work, we investigate the localization properties of a one-dimensional non-Hermitian cross-stitch flat-band lattice with mosaic quasi-periodic modulation, consisting of a constant potential and a quasi-periodic potential. When the constant potential modulation is absent, the energy spectrum is purely real and precisely determined. Moreover, the non-Hermitian skin effect is absent. When the constant potential modulation is nonzero, the system exhibits a class of exact AMEs under periodic boundary conditions (PBCs). This occurs because, through a local rotational transformation, the system forms a structure characterized by mosaic-type quasi-periodic hopping coefficients and on-site potentials, leading to the emergence of AMEs. Through rigorous derivation, we reveal that this class of models is mathematically equivalent to a generalized non-Hermitian AA model. While previous studies on generalized non-Hermitian AA models have shown an energy-independent phase transition from a critical phase to a localized phase, our model exhibits energy-dependent phase transition points. We construct energy-dependent phase transition points in this work. This key distinction explains the emergence of analytically solvable AMEs in our system. These findings reveal rich localization phenomena and provide new insights into the interplay between non-Hermitian systems and AMEs in flat-band systems. Finally, we propose an experimental scheme using electrical circuits to realize our non-Hermitian model.

The rest of the paper is organized as follows. In Section 2, we introduce the models examined in this work and discuss their common features. In Section 3, we study the localization properties of the system. An experimental scheme using electrical circuits is proposed to realize our model in Section 4. Finally, a summary is presented in Section 5.

2. Model

We consider a nonreciprocal cross-stitch flat lattice, depicted in Fig. 1. Within the tight-binding approximation, the eigenvalue equation is formulated as follows:

$$E\psi_n = -\hat{t}\psi_n - \hat{T}_1\psi_{n-1} - \hat{T}_2\psi_{n+1} + \hat{V}\psi_n, \tag{1}$$

where

$$\hat{t} = \begin{pmatrix} 0 & t \\ t & 0 \end{pmatrix}, \quad \hat{T}_1 = \begin{pmatrix} J_R & -J_R \\ J_R & -J_R \end{pmatrix},$$
$$\hat{T}_2 = \begin{pmatrix} J_L & J_L \\ -J_L & -J_L \end{pmatrix}, \quad \hat{V} = \begin{pmatrix} V_{A,n} & 0 \\ 0 & V_{B,n} \end{pmatrix}. \tag{2}$$

Here, $\hat{t}$ is the intracell coupling and t represents the intracell hopping amplitudes. $\hat{T}_1$ and $\hat{T}_2$ represent the right and left intercell coupling, respectively. Here, $J_L = Je^{h}$ and $J_R = Je^{-h}$, where J denotes the nearest neighbor hopping amplitude and h is the nonreciprocal parameter. Here, we set $J = 1$ as the unit of energy. $\hat{V}$ represent the on-site potential matrices. Here, the on-site potentials on atoms A and B are considered to have an antisymmetric form, i.e., $V_{A,n} = -V_{B,n} = V_n$. The on-site mosaic modulation V_n is defined as[28,53]

$$V_n = \begin{cases} \Delta_1 \cos(2\pi\beta n), & n = \kappa s, \\ \Delta_2, & \text{otherwise}, \end{cases} \tag{3}$$

where $\beta = (\sqrt{5}-1)/2$, Δ_1, and Δ_2 denote the quasi-periodic and constant potential amplitudes, respectively, and κ is an integer. Given that the quasi-periodic potential repeats at intervals of κ, we group the closest κ unit cells into clusters, labeled by s. If the total number of the cluster is $\tilde{N}$, the system size will be $L = 2\kappa\tilde{N}$, where $N = \kappa\tilde{N}$. If $h = 0$ and the on-site potential is set to zero, the system has two flat bands $E_\pm = \pm\sqrt{t^2+4}$.[69,70] If $h = 0$ and $\kappa = 1$, the system is subjected to AA-type potential modulation and exhibits a critical-to-insulator transition at $\Delta_1 = 4$ without showing any AMEs.[58] The vector $\psi_n = (a_n\ b_n)^{\mathrm{T}}$ corresponds to the two-site wavefunction in the n-th unit cell of the periodic lattice. By using a local coordinate transformation, the unit cells of the flat-band system can be transformed into a Fano defect form.[57] For the cross-stitch lattice, the local coordinate transformation $\hat{U}$[57] is

$$\begin{pmatrix} p_n \\ f_n \end{pmatrix} = \hat{U}\begin{pmatrix} a_n \\ b_n \end{pmatrix}, \quad \hat{U} = \frac{1}{\sqrt{2}}\begin{pmatrix} 1 & 1 \\ 1 & -1 \end{pmatrix}. \tag{4}$$

After this transformation, the eigenvalue Eq. (4) becomes

$$\begin{aligned} (E+t)p_n &= -2J_R f_{n-1} + V_n f_n, \\ (E-t)f_n &= -2J_L p_{n+1} + V_n p_n. \end{aligned} \tag{5}$$

The schematic diagram of the model described by Eq. (5) is shown in Fig. 1(b). Eliminating f_n in favor of p_n, we obtain an effective equation for p_n:

$$B_0 p_n = -2J_R V_{n-1} p_{n-1} - 2J_L V_n p_{n+1} + V_n^2 p_n \tag{6}$$

with $B_0 = E^2 - t^2 - 4$. This formulation describes a one-dimensional mosaic-modulated chain, referred to as the P-chain. The total number of the quasicell is denoted by $\tilde{N}$, and the system size of the P-chain is given by $N = \kappa\tilde{N}$.

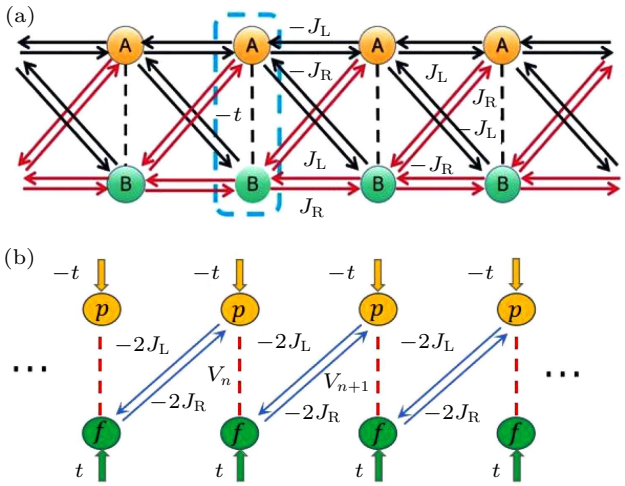


Fig. 1. (a) Schematic diagram of the non-Hermitian cross-stitch lattice. The blue dotted box region indicates the unit cell with two sublattices labeled A and B. (b) Schematic diagram of the model described by Eq. (7).

To investigate the localization properties of the eigenstates, one can calculate the inverse participation ratio (IPR),[12] $\mathrm{IPR}^{(i)} = \sum_{n=1}^{N}\sum_{\alpha=\{\mathrm{A,B}\}}|\psi_{n,\alpha}^{(i)}|^4$, where $\psi_{n,\alpha}^{(i)}$ represents the probability amplitude of the i-th eigenstate, with eigenvalue E_i, on the α sublattice in the n-th unit cell. For an extended state, the IPR tends to zero in the thermodynamic limit. Conversely, for a localized state, the IPR remains finite. For critical states, $\mathrm{IPR}^{(i)} \propto L^{-\Gamma_i}$ with $\Gamma_i \in (0,1)$. To quantify this behavior, the fractal dimension of the i-th eigenstate $\psi_{n,\alpha}^{(i)}$ is defined as[35,37,71–73]

$$\Gamma_i = -\lim_{L\to\infty}\left[\frac{\ln \mathrm{IPR}^{(i)}}{\ln L}\right]. \tag{7}$$

Based on this definition, we can see that $\Gamma_i \to 1$ for an extended state; $\Gamma_i \to 0$ for a localized state; and when $\Gamma_i \in (0,1)$, the corresponding state is a critical one. Moreover, the mean IPR can be used to identify the localization characteristics of a given region, $\mathrm{MIPR}(\tilde{\sigma}_{\tilde{\beta}}) = (1/\mathcal{N}_{\tilde{\sigma}_{\tilde{\beta}}})\sum_{i\in\tilde{\sigma}_{\tilde{\beta}}}\mathrm{IPR}^{(i)}$. Here, $(\tilde{\sigma}_{\tilde{E}})$, $(\tilde{\sigma}_{\tilde{C}})$ and $(\tilde{\sigma}_{\tilde{L}})$ correspond to extended, critical, and localized regimes, respectively, $\tilde{\beta} \in (\tilde{E},\tilde{C},\tilde{L})$. And $\mathcal{N}_{\tilde{\sigma}_{\tilde{\beta}}}$ is the total number of eigenstates in the corresponding region. The scaling behavior of MIPR is described by $\mathrm{MIPR}(\tilde{\sigma}_{\tilde{\beta}}) \propto L^{-\tilde{\Gamma}}$. For a critical region, the exponent $\tilde{\Gamma}$ lies within the interval $(0,1)$. For a localized region, $\mathrm{MIPR}(\tilde{\sigma}_{\tilde{L}})$ retains a finite value independent of the system size. Conversely, for an extended region, $\mathrm{MIPR}(\tilde{\sigma}_{\tilde{E}})$ scales linearly with $1/L$.

In this paper, we apply the exact diagonalization method to numerically calculate the nonreciprocal cross-stitch chain with $t = 1$ and $\beta = (\sqrt{5}-1)/2$.

3. Localization features

Let us first consider the case of $\Delta_2 = 0$. For any $\kappa \geq 2$, there is a $(\kappa-2)\tilde{N}$-fold degeneracy at $E = \pm\sqrt{t^2+4}$. The degeneracy of the remaining $L-2(\kappa-2)\tilde{N}$ energies is lifted, and these energies are given by

$$E = \pm\sqrt{t^2+4+V_{\kappa s}^2/2 \pm \sqrt{4V_{\kappa s}^2+V_{\kappa s}^4}/4}. \tag{8}$$

Typically, the energy spectrum of a non-Hermitian Hamiltonian is complex, and nonreciprocal hopping can induce the skin effect in a system, where the energy spectrum often forms closed loops in the complex energy plane under PBCs.[64,74] However, from the result of Eq. (8), we can see that the system's energy spectrum is purely real, indicating that the skin effect does not exist in this system. According to Fig. 1(b), when $\Delta_2 = 0$, the effective model described by Eq. (5) becomes decoupled, depending on the choice of κ, except at the bonds with nonzero mosaic potentials (Δ_1). In this scenario, the two degenerate energies in Fig. 2(a) arise from these decoupled dimers, which form $(\kappa-2)\tilde{N}$ identical 2×2 matrices describing two sites nonreciprocally coupled by J_R and J_L. Meanwhile, the other energies in Eq. (8) result from two dimers coupled by mosaic potentials, described by a 4×4 matrix depending on $V_{\kappa s}$. Therefore, the energy spectrum of the system is entirely real and the non-Hermitian skin effect is absent.

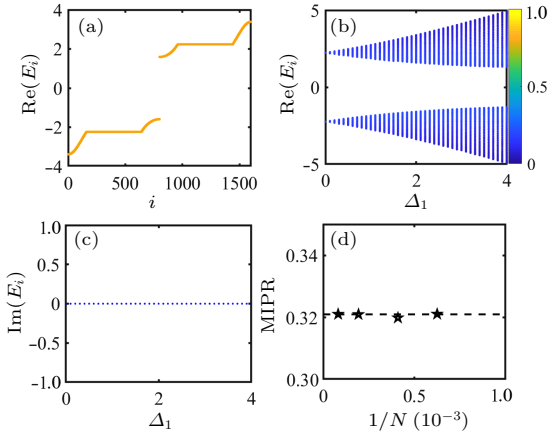


Fig. 2. (a) The energy distributions with $\Delta_1 = 2$ and $N = 800$ under PBCs, respectively. (b) The fractal dimension Γ_i of different eigenstates as a function of the corresponding real part of E_i and Δ_1 with $N = 800$ under PBCs. (c) The image part of E_i as a function of Δ_1 with $N = 800$ under PBCs. (d) The MIPR as a function of $1/N$ with Δ_1=3. Other parameters: $\kappa = 5$, $h = 0.1$, $t = 1$ and $\Delta_2 = 0$.

Here, we select $\kappa = 5$ to numerically validate the above conclusion. Figure 2(a) presents the real part of the energy distributions for $\Delta_1 = 2$ and $N = 800$. A 480-fold degeneracy is observed at $E = \pm\sqrt{5}$. The non-degenerate energy values in Fig. 2(a) align well with those predicted by Eq. (8), confirming the accuracy of our numerical results. To address the effects of this degeneracy, we introduce a small random perturbation at each site, with the perturbation amplitude set to 10^{-8}, as shown in Figs. 2(b)–2(d). Figure 2(b) displays the fractal dimension Γ_i of different eigenstates as a function of the real part of E_i and Δ_1 under PBCs. Notably, regardless of

variations in the quasi-periodicity strength, the Γ_i values for all states approach 0, indicating that the system remains in a localized phase when $\Delta_2 = 0$. The imaginary part of E_i remains zero at all times, as illustrated in Fig. 2(c). Furthermore, the scaling behavior of the MIPR is shown in Fig. 2(d), where it can be seen that the MIPR values converge to a finite value in the thermodynamic limit.

To intuitively verify that there is no skin effect in the system, we selected three different eigenstates from the band-edge and band-center regions under open boundary conditions (OBCs) and plotted the corresponding space distributions in Figs. 3(a)–3(c). From Figs. 3(a)–3(c), one can see that the eigenstates are localized states and nonreciprocal hopping does not induce a skin effect in $\Delta_2 = 0$.

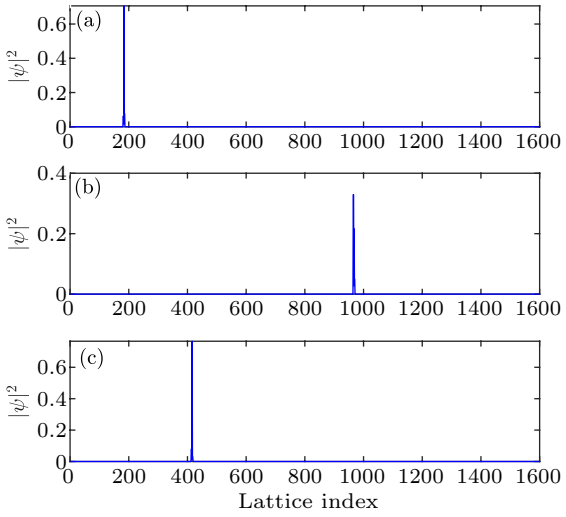


Fig. 3. (a)–(c) The eigenstates spatial distributions with $E = -3.3181$, 1.5741, and 4.0071 under open boundary conditions, respectively. Here, $N = 800$, $h = 0.1$, $t = 1$, $\Delta_2 = 0$ and $\Delta_1 = 3$.

For the case of $\Delta_2 \neq 0$, the system exhibits distinct localization properties, and the AMEs emerge. Here, we choose $\kappa = 2$ and 3 as nontrivial examples to discuss.

For $\kappa = 2$, the quasi-periodic potential is set on even unit cells. The exact expression for AMEs is given by (with a detailed derivation provided in Appendix B)

$$E_c = \pm\sqrt{\pm\frac{8\Delta_2 J_L^2}{\Delta_1} + t^2 + \Delta_2^2}, \tag{9}$$

which is marked by the red solid lines in Fig. 4(a). AMEs are not only the boundaries between localized and critical states in the system but also the dividing lines between the real and complex parts of the energy spectrum, as shown in Appendix A. Figure 4(a) displays Γ_i as a function of the real part of E_i and Δ_1 for $N = 610$. The yellow and blue regions represent critical and localized states, respectively. In the weak disorder regime, the Γ_i values for all eigenstates deviate from 0 and 1, suggesting that the system is in a critical phase. As Δ_1 increases to 2, a pair of AMEs appears, signaling the transition from the critical phase to a mixed phase of critical and localized states. When $\Delta_1 \approx 5$, another pair of AMEs emerges. It is evident that four AMEs are present in the strong disorder region. Notably, critical states remain robust in the strong disorder regime with large disorder, particularly for the case of $\kappa = 2$.

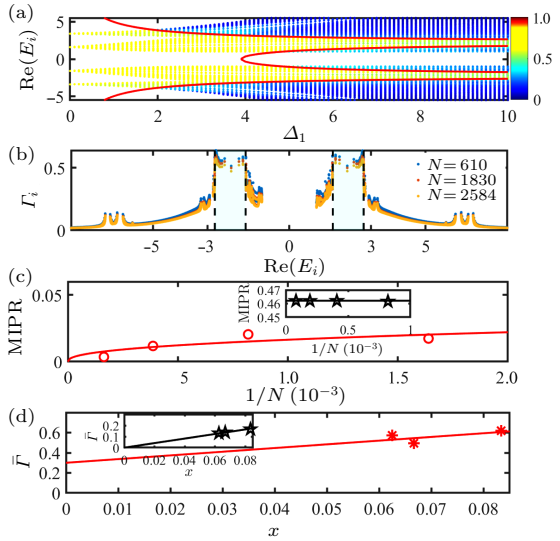


Fig. 4. (a) The fractal dimension Γ_i of different eigenstates as a function of the corresponding real part of E_i and Δ_1 for $N = 610$ under PBCs. The red lines represent the AMEs given in Eq. (9). (b) The fractal dimension Γ_i versus real part of E_i and different system sizes for $\Delta_1 = 8$. The black dashed lines represent eigenstate indices of the AMEs given by Eq. (9). (c) The MIPR for the critical regions as a function $1/N$. The insets show the scalings of the MIPR for the corresponding localized regions. (d) Mean fractal dimensions $\overline{\Gamma}$ as a function of x for the critical region with $\Delta_1 = 8$. The inset shows the scaling of $\overline{\Gamma}$ for the corresponding localized regions. Here, $x = 1/m$ with m being the index of the Fibonacci number F_m. Other parameters: $t = 1$, $\kappa = 2$, $\Delta_2 = 2$ and $h = 0.1$.

Figure 4(b) displays the fractal dimensions Γ_i as a function of system size for $\Delta_1 = 8$. The black dashed lines indicate the positions of the AMEs, as determined by Eq. (9). In the shaded regions, the values of Γ_i deviate from 0 and 1 for different system sizes. In contrast, within the region between the two analytical AMEs, the values of Γ_i approach 0, indicating that these states are localized. Figure 4(c) illustrates the scaling behavior of the MIPR across different regions. The scaling of the MIPR in the critical regions is fitted as $\mathrm{MIPR}_{\tilde{C}} \approx 0.3103(1/N)^{0.4254}$. The scaling behavior of the MIPR in the localized regions is shown in the insets of Fig. 4(c), where it demonstrates system-size-independent behavior, with $\mathrm{MIPR}_{\tilde{L}}$ approaching a constant value in the thermodynamic limit. Moreover, the mean fractal dimension of a specific region, $\overline{\Gamma}$ can also be used to characterize the localization properties of a system in the thermodynamic limit, which is defined as $\overline{\Gamma}(\tilde{\sigma}_{\tilde{\beta}}) = (1/\mathcal{N}_{\tilde{\sigma}_{\tilde{\beta}}})\sum_{i\in\tilde{\sigma}_{\tilde{\beta}}}\Gamma_i$.[28,39] For a localized region, $\overline{\Gamma}$ approaches 0 in the thermodynamic limit. For an extended region, $\overline{\Gamma}$ approaches 1 as the system size increases.

In a critical region, the value of $\overline{\Gamma}$ approaches a finite value within the interval $(0,1)$ as the system reaches the thermodynamic limit.[28,39] Figure 4(d) illustrates the finite-size scaling of $\overline{\Gamma}$ for critical and localized regions, respectively. Here, $x = 1/m$, where m is the index of the Fibonacci number F_m, defined by $F_{m+1} = F_m + F_{m-1}$ and $F_1 = F_0 = 1$, and the corresponding system size is $N = 2F_m$. As shown in Fig. 4(d), the value of $\overline{\Gamma}(\tilde{C})$ converges to 0.3 for the critical regime in the thermodynamic limit. In contrast, $\overline{\Gamma}(\tilde{L})$ for localized regions decays linearly with the system size and asymptotically approaches zero in the thermodynamic limit, as shown in the inset of Fig. 4(d).

The results above were obtained under PBCs. How would the localization properties of the system change if OBCs were applied? Due to the presence of non-reciprocal coupling, the system exhibits the skin effect under OBCs, which leads to localized features. Consequently, traditional order parameters, such as the fractal dimension Γ_i, struggle to differentiate between skin states and conventional localized states. To address this issue, we introduce the mean center of mass (MCM),[75] defined as $\mathrm{MCM} = \sum_{n=1}^{N} n\left(|a_n|^2 + |b_n|^2\right)$. Figure 5 shows the MCM as a function of Δ_1 and the real part of E_i for $N = 610$, $h = 0.1$, and $\Delta_2 = 2$ under OBCs. The black solid lines represent the analytical results from Eq. (9). The minimum value of the MCM in the central region of the analytical solution indicates that the wave function is localized at the left boundary, corresponding to left skin states. In contrast, the outer region exhibits much larger values, indicating localized features that are unaffected by non-reciprocal hopping. This demonstrates that critical states under PBCs transform into left skin states under OBCs, while localized states maintain their localization characteristics under OBCs.

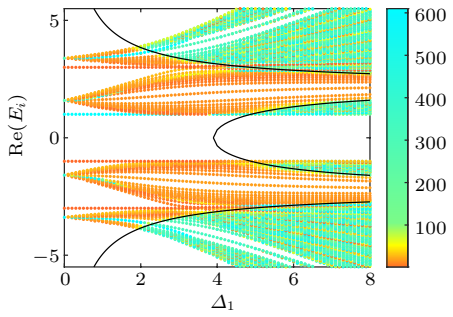


Fig. 5. The mean center of mass (MCM) of different eigenstates as a function of the corresponding real part of E_i and Δ_1 for $N = 610$ under OBCs. The black lines represent the AMEs given in Eq. (9). Other parameters: $t = 1$, $\kappa = 2$, $\Delta_2 = 2$ and $h = 0.1$.

For an arbitrary κ, the exact expression for AMEs (with a detailed derivation provided in Appendix B) is given by

$$2\left|\frac{(-2J_{\mathrm{L}})^{\kappa}(\Delta_2)^{\kappa-1}\Delta_1}{\prod_m^{\kappa-1} A_m}\right| = \left|\left(\frac{4}{A_{\kappa-1}}+1\right)\Delta_1^2\right|, \quad (10)$$

where $A_m = A_1 - \frac{(-2\Delta_2)^2}{A_{m-1}}$, $A_1 = E^2 - t^2 - 4 - \Delta_2^2$. For $\kappa = 3$, Eq. (10) simplifies to

$$E_{\mathrm{c}} = \pm\sqrt{2 + t^2 + \Delta_2^2 \pm \sqrt{4 + 4\Delta_2^2 \pm \frac{16J_{\mathrm{L}}^3}{\Delta_1}\Delta_2^2}}, \quad (11)$$

The above results are presented in Fig. 6(a), with the red solid lines marking the positions of the AMEs. In this figure, Γ_i is plotted as a function of Δ_1 for $N = 630$. As predicted by the analytical results, the values of Γ_i exhibit a sharp change when the energies cross these red lines. To illustrate the changes in Γ_i for different system sizes, we use $\Delta_1 = 5$ as a specific example in Fig. 6(b). The black dashed lines indicate the AMEs as given by Eq. (11). It is evident that the Γ_i values of the eigenstates in the shaded region deviate substantially from 0 and 1 as the system size increases, suggesting that these states are critical. Similarly, we calculate the MIPR for a specific region as a function of $1/N$, as shown in Fig. 6(c). The scaling of the MIPR in the two critical regions follows the form $\mathrm{MIPR}_{\tilde{C}} \approx 0.1062(1/N)^{0.3101}$, demonstrating critical behavior. The scaling of the MIPR in the localized regions is shown in the insets of Fig. 6(c), where it approaches a constant value. Furthermore, for any κ, one can derive $4(\kappa-1)$ AMEs, as described in Eq. (10). We also show the scaling of $\overline{\Gamma}$ for specific regions, as shown in Fig. 6(d) with $N = 3F_m$. It is observed that $\overline{\Gamma}$ approaches 0.45 in the thermodynamic limit for the critical region. In the localized region, $\overline{\Gamma}$ exhibits a linear decay with increasing system size and tends to zero in the thermodynamic limit, as demonstrated in the inset of Fig. 6(d).

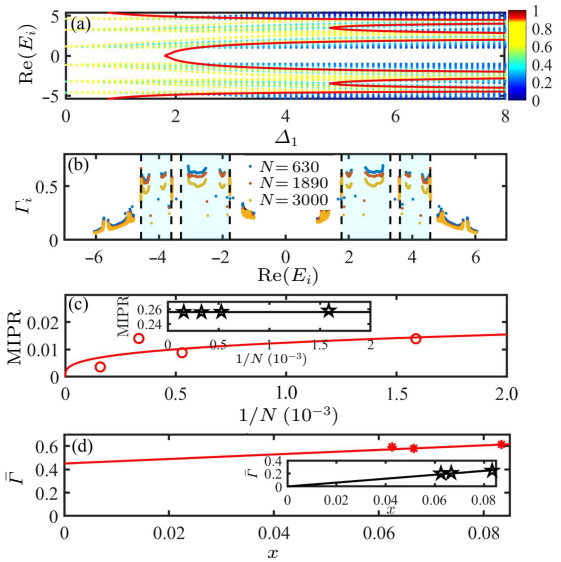


Fig. 6. (a) The fractal dimension Γ_i of different eigenstates as a function of real part of E_i and Δ_1 for $N = 630$. The red lines represent the AMEs given in Eq. (11). (b) The fractal dimension Γ_i versus real part of E_i and different system sizes for $\Delta_1 = 5$. The black dashed lines represent eigenstate indices of the AMEs given by Eq. (11). (c) The MIPR for the critical regions as a function $1/N$ for $\Delta_1 = 5$. The insets show the scalings of the MIPR for the corresponding localized regions. (d) $\overline{\Gamma}$ as a function of x for the critical region with $\Delta_1 = 5$. The inset in (d) shows the scaling of $\overline{\Gamma}$ for localized regions. Other parameters: $t = 1$, $\kappa = 3$, $\Delta_2 = 3$ and $h = 0.1$.

To clearly demonstrate the robustness of AMEs even in the presence of random perturbations, we introduced a small random disorder into the quasi-periodic mosaic potential. In Fig. 7, we plot the fractal dimension Γ_i of different eigenstates as a function of the corresponding E_i and Δ_1, incorporating small random perturbations in the quasi-periodic mosaic potential for (a) $\kappa = 2$ and (b) $\kappa = 3$. Specifically, the amplitude of the random disorder is set to 10^{-3}. Nevertheless, as shown in Fig. 7, AMEs persist in the system even in the presence of random perturbations. However, the analytical expression for the AMEs no longer accurately predicts their exact positions, indicating that random perturbations cause a shift in their location. These results indicate that the random perturbations only influence the location of AMEs within the system.

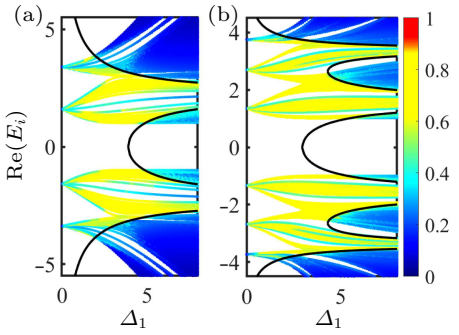


Fig. 7. The fractal dimension Γ_i of different eigenstates as a function of the corresponding E_i and Δ_1 with small random perturbations in quasi-periodic mosaic potential for (a) $\kappa = 2$ and (b) $\kappa = 3$. The black lines represent the AMEs given in Eqs. (9) and (11) without small random perturbations in (a) and (b). Other parameters: (a) $N = 610$, (b) $N = 630$, $\Delta_2 = 2$ and $h = 0.1$.

4. Experimental realization

We designed an electrical circuit in Fig. 8(a), corresponding to the system described by Eq. (1). The nonreciprocal hopping between cells is simulated by combining an INIC, as shown in Figs. 8(b). The INIC consists of a normal capacitor C_γ and a capacitor C_λ, one operational amplifier, and two resistors with equal resistance values R'. When the current flows from left to right, the capacitance between the nodes of this cell and the nodes of the next cell is $C_\gamma - C_\lambda$. If the current runs in the opposite direction, the capacitance will be $C_\gamma + C_\lambda$. The capacitor C_t is utilized to represent the intracell hopping of the model in Eq. (4). The inductor $\mathcal{L}$ is used to tune the resonant frequency of the circuit, and the on-site potentials at each site are simulated by grounding capacitors C_n^a and C_n^b. This system described by Eq. (4) can be represented by the circuit Laplacian $\mathcal{J}(\omega)$. The Laplacian is defined as the response of the grounded-voltage vector $\mathcal{V}$ to the vector I of input current by

$$I(\omega) = \mathcal{J}(\omega)\mathcal{V}(\omega). \tag{12}$$

Using Eq. (12), the current of each node within the unit cell can be expressed as

$$\begin{aligned}
I_n^a &= \mathrm{i}\omega C_t \mathcal{I}_2 \mathcal{V}_n^b + \mathrm{i}\omega\Big[(C_\gamma + C_\lambda)(\mathcal{V}_{n+1}^a + \mathcal{V}_{n+1}^b) \\
&\quad + (C_\gamma - C_\lambda)\mathcal{V}_{n-1}^a\Big]\begin{pmatrix} 0 & 1 \\ 1 & 0 \end{pmatrix} + \mathrm{i}\omega(C_\gamma - C_\lambda)\mathcal{I}_2\mathcal{V}_{n-1}^b \\
&\quad + \left[\frac{1}{\mathrm{i}\omega\mathcal{L}}\begin{pmatrix} -1 & 1 \\ 1 & -1 \end{pmatrix} - \mathrm{i}\omega\Big(C_{n,a} + C_t + 4C_\gamma\Big)\mathcal{I}_2\right]\mathcal{V}_n^a, \\
I_n^b &= \mathrm{i}\omega C_t \mathcal{I}_2 \mathcal{V}_n^a + \mathrm{i}\omega(C_\gamma - C_\lambda)\begin{pmatrix} 0 & 1 \\ 1 & 0 \end{pmatrix}\mathcal{V}_{n-1}^a \\
&\quad + \mathrm{i}\omega\mathcal{I}_2\Big[(C_\gamma + C_\lambda)(\mathcal{V}_{n+1}^b + \mathcal{V}_{n+1}^a) + (C_\gamma - C_\lambda)\mathcal{V}_{n-1}^b\Big] \\
&\quad + \left[\frac{1}{\mathrm{i}\omega\mathcal{L}}\begin{pmatrix} -1 & 1 \\ 1 & -1 \end{pmatrix} - \mathrm{i}\omega\Big(C_{n,b} + C_t + 4C_\gamma\Big)\mathcal{I}_2\right]\mathcal{V}_n^b,
\end{aligned} \tag{13}$$

where the vectors $I_n^\alpha = (I_{n,1}^\alpha, I_{n,2}^\alpha)^{\mathrm{T}}$ $(\alpha = a,b)$ and $\mathcal{V}_n^\alpha = (\mathcal{V}_{n,1}^\alpha, \mathcal{V}_{n,2}^\alpha)^{\mathrm{T}}$ $(\alpha = a,b)$ represent the node currents and voltages of the a and b sublattices within the nth unit cell, respectively, and $\mathcal{I}_2$ represents the 2×2 identity matrix. We transform Eq. (13) using a unitary matrix

$$U = \frac{1}{\sqrt{2}}\begin{pmatrix} 1 & 1 \\ 1 & -1 \end{pmatrix}, \tag{14}$$

and obtain the transformed current–voltage relationship

$$\begin{aligned}
\tilde{I}_n^a &= \mathrm{i}\omega C_t \mathcal{I}_2 \tilde{\mathcal{V}}_n^b + \mathrm{i}\omega\begin{pmatrix} 1 & 0 \\ 0 & -1 \end{pmatrix}\Big[(C_\gamma + C_\lambda)(\tilde{\mathcal{V}}_{n+1}^a \\
&\quad + \tilde{\mathcal{V}}_{n+1}^b) + (C_\gamma - C_\lambda)\tilde{\mathcal{V}}_{n-1}^a\Big] + \mathrm{i}\omega(C_\gamma - C_\lambda)\mathcal{I}_2\tilde{\mathcal{V}}_{n-1}^b \\
&\quad + \left[\frac{1}{\mathrm{i}\omega\mathcal{L}}\begin{pmatrix} 0 & 0 \\ 0 & -2 \end{pmatrix} - \mathrm{i}\omega\Big(C_{n,a} + C_t + 4C_\gamma\Big)\mathcal{I}_2\right]\tilde{\mathcal{V}}_n^a, \\
\tilde{I}_n^b &= \mathrm{i}\omega C_t \mathcal{I}_2 \tilde{\mathcal{V}}_n^a + \mathrm{i}\omega(C_\gamma - C_\lambda)\begin{pmatrix} 1 & 0 \\ 0 & -1 \end{pmatrix}\tilde{\mathcal{V}}_{n-1}^a \\
&\quad + \mathrm{i}\omega\mathcal{I}_2\Big[(C_\gamma + C_\lambda)(\tilde{\mathcal{V}}_{n+1}^b + \tilde{\mathcal{V}}_{n+1}^a) + (C_\gamma - C_\lambda)\tilde{\mathcal{V}}_{n-1}^b\Big] \\
&\quad + \left[\frac{1}{\mathrm{i}\omega\mathcal{L}}\begin{pmatrix} 0 & 0 \\ 0 & -2 \end{pmatrix} - \mathrm{i}\omega\Big(C_{n,b} + C_t + 4C_\gamma\Big)\mathcal{I}_2\right]\tilde{\mathcal{V}}_n^b.
\end{aligned} \tag{15}$$

We rewrite the current-voltage equations for the second nodes as

$$\begin{aligned}
\tilde{I}_{n,2}^a &= \mathrm{i}\omega C_t \tilde{\mathcal{V}}_{n,2}^b - \mathrm{i}\omega\Big[(C_\gamma + C_\lambda)(\tilde{\mathcal{V}}_{n+1,2}^a + \tilde{\mathcal{V}}_{n+1,2}^b) \\
&\quad + (C_\gamma - C_\lambda)\tilde{\mathcal{V}}_{n-1,2}^a\Big] + \mathrm{i}\omega(C_\gamma - C_\lambda)\tilde{\mathcal{V}}_{n-1,2}^b \\
&\quad + \mathrm{i}\omega\left[\frac{2}{\omega^2\mathcal{L}} - \Big(C_{n,a} + C_t + 4C_\gamma\Big)\right]\tilde{\mathcal{V}}_{n,2}^a, \\
\tilde{I}_{n,2}^b &= \mathrm{i}\omega C_t \tilde{V}_{n,2}(a) - \mathrm{i}\omega(C_\gamma - C_\lambda)(\tilde{\mathcal{V}}_{n-1,2}^a - \tilde{\mathcal{V}}_{n-1,2}^b) \\
&\quad + \mathrm{i}\omega(C_\gamma + C_\lambda)(\tilde{\mathcal{V}}_{n+1,2}^b + \tilde{\mathcal{V}}_{n+1,2}^a) \\
&\quad + \mathrm{i}\omega\left[\frac{2}{\omega^2\mathcal{L}} - \Big(C_{n,b} + C_t + 4C_\gamma\Big)\right]\tilde{\mathcal{V}}_{n,2}^b,
\end{aligned} \tag{16}$$

where $\tilde{I}_{n,2}(\alpha)$ and $\tilde{V}_{n,2}(\alpha)$ $(\alpha = a,b)$ denote the current and voltage of the second node within each sublattice in the circuit. Therefore, we achieve the targeted circuit Laplacian $\mathcal{J}(\omega)$ to simulate the system in Eq. (1) as

$$J(\omega)=\mathrm{i}\omega\begin{pmatrix} -C_{1,a} & C_t & -C_\gamma-C_\lambda & -C_\gamma-C_\lambda & \dots & 0 \\ C_t & -C_{1,b} & C_\gamma+C_\lambda & C_\gamma+C_\lambda & \dots & 0 \\ -C_\gamma+C_\lambda & C_\gamma-C_\lambda & -C_{2,a} & C_t & \dots & 0 \\ -C_\gamma+C_\lambda & C_\gamma-C_\lambda & C_t & -C_{2,b} & \dots & \vdots \\ \vdots & \vdots & \vdots & \ddots & \ddots & C_t \\ 0 & 0 & 0 & \dots & C_t & -C_{n,b} \end{pmatrix}+\left(\frac{2}{(\omega)^2L}-C_t-4C_\gamma\right)\mathcal{I}_{2n}, \tag{17}$$

where $\mathcal{I}_{2n}$ represents the $2n\times 2n$ identity matrix. Hence, the system for the non-Hermitian cross-stitch flat band lattice with an on-site mosaic quasi-periodic modulation is achieved. The energy spectrum of the system can be obtained from the admittance spectrum of the circuit, and the distribution of states can be detected by measuring the voltage at each node.[76,77]

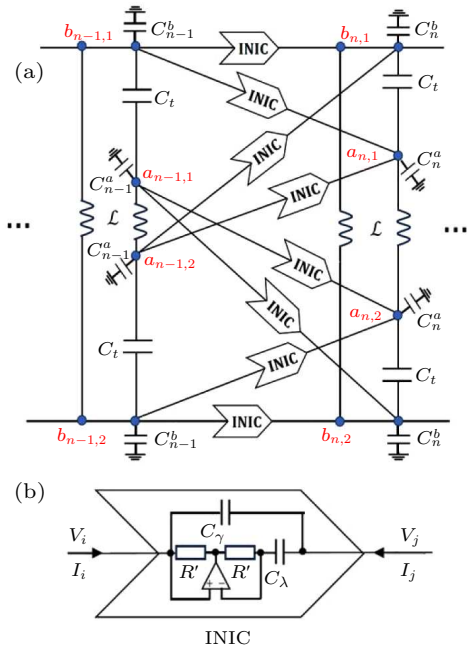


Fig. 8. (a) Electrical circuit implementation of the model in Eq. (1). (b) The details of the INIC.

5. Summary

In this study, we investigated the localization transition in a nonreciprocal cross-stitch lattice with quasi-periodic mosaic modulations. When $\Delta_2=0$, the non-Hermitian skin effect does not occur. Moreover, through analytical derivation, we determine that the system's energy spectrum is purely real. This is different from typical non-Hermitian systems, where the energy spectrum is generally complex. However, when $\Delta_2\neq 0$, we present a simpler method to derive a general solution for a class of AMEs under PBCs. Under OBCs, the AMEs transform into boundaries that distinguish between localized states and skin states. Moreover, from analytical results, we find that the system with AMEs induced by the mosaic is fundamentally equivalent to a generalized non-Hermitian AA model. According to the conclusions drawn from the generalized non-Hermitian AA model, a transition from a critical phase to a localized phase exists. However, our analysis reveals that the transition point from the critical phase to the localized phase is energy-dependent, which fundamentally accounts for the emergence of AMEs in our study. Thus, we have provided a further physical explanation for the existence of AMEs. Moreover, we propose an experimental realization using electrical circuits, providing a practical platform for realizing our system, along with circuit diagrams and detailed derivations. Our findings offer new insights into AMEs in non-Hermitian flat band systems.

Appendix A: The change of the spectrum for $\Delta_2\neq 0$

We consider the case of $\kappa=2$. In Figs. A1(a) and A1(b), we plot the $\ln|\mathrm{Im}(E_i)|$ as a function of $\mathrm{Re}(E_i)$ and Δ_1 under OBCs and PBCs, respectively. One can see that AMEs are not only the boundaries between localized and critical states in the system but also the dividing lines between the real and complex parts of the energy spectrum, as shown in Fig. A1(b). The critical states in the system correspond to complex energy spectra. We find that under OBCs, the critical states transform into skin states, and their energies change from complex to real, as shown in Fig. A1(a). In contrast, the localized states maintain purely real energies, as shown in Figs. A1(a) and A1(b). In nonreciprocal systems, under PBCs, the complex energy spectrum forms complex energy loops in the energy parameter space, corresponding to a nontrivial spectral topology. Under OBCs, the eigenstates associated with these complex spectra exhibit the non-Hermitian skin effect,[66,67] as shown in Fig. 5.

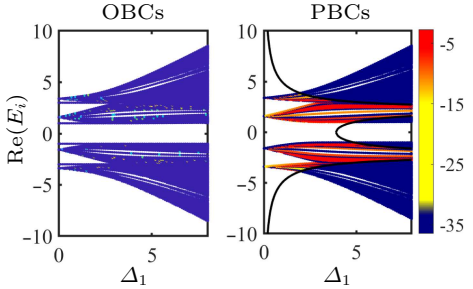


Fig. A1. The $\ln|\mathrm{Im}(E_i)|$ of different eigenstates as a function of the corresponding real part of E_1 and Δ_1 for $N=610$ under (a) OBCs and (b) PBCs. Here, the color denotes the value of $\ln|\mathrm{Im}(E_i)|$. The black lines represent the AMEs given in Eq. (9). Other parameters: $t=1$, $\kappa=2$, $\Delta_2=2$ and $h=0.1$.

Appendix B: Arbitrary κ case for $\Delta_2 \neq 0$

We begin by considering the case of $\kappa = 2$. In this case, the on-site potential is quasi-periodic at the $2s$-th unit cells, while at other unit cells, it remains a constant with a potential $\Delta_2 \neq 0$. From Eq. (8), the effective eigenvalue equations for the P-chain can be expressed as

$$\begin{aligned} A_1 p_{1,s} &= -2J_R V_{2,s-1} p_{2,s-1} - 2J_L \Delta_2 p_{2,s} \\ B_0 p_{2,s} &= -2J_R \Delta_2 p_{1,s} - 2J_L V_{2,s} p_{1,s+1} + V_{2,s}^2 p_{2,s}, \end{aligned} \tag{B1}$$

where $A_1 = B_0 - \Delta_2^2$. Here, the subscripts of $p_{\tilde{\alpha},s}$ and $V_{\tilde{\alpha},s}$ denote the $\tilde{\alpha}$-th site in the s-th quasicell, with $\tilde{\alpha} = 1, 2, \ldots, \kappa$ and $s = 1, 2, \ldots, \tilde{N}$. By reducing Eq. (B1), we obtain

$$\begin{aligned} \left(B_0 - \frac{4\Delta_2^2}{A_1}\right) p_{2,s} = &\frac{4\Delta_2 J_R^2}{A_1} V_{2,s-1} p_{2,s-1} + \frac{4\Delta_2 J_L^2}{A_1} V_{2,s} p_{2,s+1} \\ &+ \left(\frac{4}{A_1} + 1\right) V_{2,s}^2 p_{2,s}. \end{aligned} \tag{B2}$$

This eigenvalue equation, Eq. (B2), represents a one-dimensional generalized nonreciprocal AA model with quasiperiodically modulated hopping and on-site terms. Based on the localization transition of the generalized nonreciprocal AA model,[32,59] the analytical expressions for the AMEs are given by

$$\left|\left(\frac{4J^2}{A_1} + 1\right)\Delta_1\right| = \left|\frac{2\Delta_2}{A_1} M^2\right|, \tag{B3}$$

where $M^2 = \mathrm{Max}\{(-2J_L)^2, (-2J_R)^2\}$. Here, we consider $J_L > J_R$. So Eq. (B3) can be further simplified as

$$E_c = \pm\sqrt{\pm\frac{8\Delta_2 J_L^2}{\Delta_1} + t^2 + \Delta_2^2}, \tag{B4}$$

which are represented by the solid lines in Figs. 4(a) and 5.

Then, we consider the case of $\kappa = 3$. Similarly, Eq. (8) for the P-chain can be expressed as

$$A_1 p_{1,s} = -2J_R V_{3,s-1} p_{3,s-1} - 2J_L V_{1,s} p_{2,s}, \tag{B5}$$

$$A_1 p_{2,s} = -2J_R V_{1,s} p_{1,s} - 2J_L V_{2,s} p_{3,s}, \tag{B6}$$

$$B_0 p_{3,s} = -2J_R V_{2,s} p_{2,s} - 2J_L V_{3,s} p_{1,s+1} + V_{3,s}^2 p_{3,s}. \tag{B7}$$

Here, $A_1 = B_0 - \Delta_2^2$. Combining Eqs. (B5) and (B6), we obtain

$$\begin{aligned} \left[A_1 - \frac{(-2\Delta_2)^2}{A_1}\right] p_{1,s} = &-2J_R V_{3,s-1} p_{3,s-1} \\ &+ \frac{(-2J_L\Delta_2)^2}{A_1} p_{3,s}, \end{aligned} \tag{B8}$$

$$\begin{aligned} \left[A_1 - \frac{(-2\Delta_2)^2}{A_1}\right] p_{2,s} = &-2\frac{-2J_R\Delta_2}{A_1} J_R V_{3,s-1} p_{3,s-1} \\ &- 2J_L\Delta_2 p_{3,s}. \end{aligned} \tag{B9}$$

Next, by combining the results of Eqs. (B7)–(B9), we arrive at the following equation:

$$\begin{aligned} \left(B_0 - \frac{4\Delta_2^2}{A_2}\right) p_{3,s} = &-\frac{8J_R^3\Delta_2^2}{A_1 A_2} V_{3,s-1} p_{3,s-1} - \frac{8J_L^3\Delta_2^2}{A_1 A_2} V_{3,s} p_{3,s+1} \\ &+ \left(\frac{4}{A_2} + 1\right) V_{3,s}^2 p_{3,s}, \end{aligned} \tag{B10}$$

where $A_2 = A_1 - \frac{(-2\Delta_2)^2}{A_1}$. Based on the localization transition point of the generalized nonreciprocal AA model,[32,59] the expression for the AMEs is given by

$$2\left|\frac{-8\Delta_2^2\Delta_1}{A_1 A_2} M^3\right| = \left|\left(\frac{4}{A_2} + 1\right)\Delta_1^2\right|, \tag{B1}$$

where $M^3 = \mathrm{Max}\{(-2J_L)^3, (-2J_R)^3\}$. Here, we consider $J_L > J_R$. Simplifying Eq. (B1), we obtain the AMEs

$$E_c = \pm\sqrt{2 + t^2 + \Delta_2^2 \pm \sqrt{4 + 4\Delta_2^2 \pm \frac{16J_L^3}{\Delta_1}\Delta_2^2}}, \tag{B12}$$

which are represented by the red solid lines in Fig. 6(a).

For any κ, the effective eigenvalue equations for the P-chain can be expressed as

$$\begin{aligned} A_1 p_{1,s} &= -2J_R V_{\kappa,s-1} p_{\kappa,s-1} - 2J_L V_{1,s} p_{2,s}, \\ &\ldots \\ B_0 p_{\kappa,s} &= -2J_R V_{\kappa-1,s} p_{\kappa-1,s} - 2J_L V_{\kappa,s} p_{1,s+1} + V_{\kappa,s}^2 p_{\kappa,s}. \end{aligned} \tag{B13}$$

Following a similar process as in the $\kappa = 2$ and 3 cases, and employing inductive reasoning, we derive

$$\begin{aligned} B_0 p_{\kappa,s} = &\frac{(-2J_R)^\kappa (\Delta_2)^{\kappa-1}}{\prod_m^{\kappa-1} A_m} V_{\kappa,s-1} p_{\kappa,s-1} \\ &+ \frac{(-2J_L)^\kappa (\Delta_2)^{\kappa-1}}{\prod_m^{\kappa-1} A_m} V_{\kappa,s} p_{\kappa,s+1} \\ &+ \frac{(-2\Delta_2)^2}{A_{\kappa-1}} p_{\kappa,s} + \left(\frac{4}{A_{\kappa-1}} + 1\right) V_{\kappa,s}^2 p_{\kappa,s}. \end{aligned} \tag{B14}$$

The corresponding expression for the AMEs is

$$2\left|\frac{(-2)^\kappa (\Delta_2)^{\kappa-1}\Delta_1}{\prod_m^{\kappa-1} A_m} M^\kappa\right| = \left|\left(\frac{4}{A_{\kappa-1}} + 1\right)\Delta_1^2\right|, \tag{B15}$$

where $A_m = A_1 - \frac{(-2\Delta_2)^2}{A_{m-1}}$ and $M^\kappa = \mathrm{Max}\{(-2J_L)^\kappa, (-2J_R)^\kappa\}$. Here $J_L > J_R$. The result of (B15) can be further simplified as

$$2\left|\frac{(-2)^\kappa (\Delta_2)^{\kappa-1}\Delta_1}{\prod_m^{\kappa-1} A_m} J_L^\kappa\right| = \left|\left(\frac{4}{A_{\kappa-1}} + 1\right)\Delta_1^2\right|. \tag{B16}$$

Acknowledgements

This work is supported by the National Natural Science Foundation of China (Grant Nos. 12375016 and 12461160324), Beijing National Laboratory for Condensed Matter Physics (Grant No. 2023BNLCMPKF001), and the Fundamental Research Program of Shanxi Province (Grant No. 202403021212025).

References

[1] Anderson P W 1958 *Phys. Rev.* **109** 1492
[2] Lee P A and Ramakrishnan T V 1985 *Rev. Mod. Phys.* **57** 287
[3] Billy J, Josse V, Zuo Z, Bernard A, Hambrecht B, Lugan P, Clément D, Sanchez-Palencia L, Bouyer P and Aspect A 2008 *Nature* **453** 891
[4] Roati G, D'Errico C, Fallani L, Fattori M, Fort C, Zaccanti M, Modugno G, Modugno M and Inguscio M 2008 *Nature* **453** 895
[5] Chabanov A A, Stoytchev M and Genack A Z 2000 *Nature* **404** 850
[6] Pradhan P and Sridhar S 2000 *Phys. Rev. Lett.* **85** 2360
[7] Lahini Y, Pugatch R, Pozzi F, Sorel M, Morandotti R, Davidson N and Silberberg Y 2009 *Phys. Rev. Lett.* **103** 013901
[8] Mott N 1987 *J. Phys. C* **20** 3075
[9] Aubry S and André G 1980 *Ann. Isr. Phys. Soc.* **3** 133
[10] Harper P G 1955 *Proc. Phys. Soc. London Sect. A* **68** 874
[11] Longhi S 2019 *Phys. Rev. B* **100** 125157
[12] Roy S, Mishra T, Tanatar B and Basu S 2021 *Phys. Rev. Lett.* **126** 106803
[13] Padhan A, Giri M K, Mondal S and Mishra T 2022 *Phys. Rev. B* **105** L220201
[14] Zuo Z W and Kang D W 2022 *Phys. Rev. A* **106** 013305
[15] Aditya S, Sengupta K and Sen D 2023 *Phys. Rev. B* **107** 035402
[16] Roy S, Chattopadhyay S, Mishra T and Basu S 2022 *Phys. Rev. B* **105** 214203
[17] Nair P S, Joy D and Sanyal S 2023 arXiv:2302.14053
[18] Wu C H, Fan J T, Chen G and Jia S T 2021 *New J. Phys.* **23** 123048
[19] Zhou L W and Han W Q 2022 *Phys. Rev. B* **106** 054307
[20] Han W Q and Zhou L W 2022 *Phys. Rev. B* **105** 054204
[21] Wang H Y, Zheng X H, Chen J, Xiao L T, Jia S T and Zhang L 2023 *Phys. Rev. B* **107** 075128
[22] Guan E G, Wang G, Guan X W and Cai X M 2023 *Phys. Rev. A* **108** 033305
[23] Goblot V, Štrkalj A, Pernet N, Lado J L, Dorow C, Lemaître A, Gratiet L L, Harouri A, Sagnes I, Ravets S, Amo A, Bloch J and Zilberberg O 2020 *Nat. Phys.* **16** 832
[24] Zhai L J, Huang G Y and Yin S 2021 *Phys. Rev. B* **104** 014202
[25] Dai Q, Lu Z P and Xu Z H 2023 *Phys. Rev. B* **108** 144207
[26] Guo C Y 2024 *Phys. Rev. B* **109** 174203
[27] Liu T, Xia X, Longhi S and Sanchez-Palencia L 2022 *Sci-Post Phys.* **12** 027
[28] Zhou X C, Wang Y J, Poon T F J, Zhou Q and Liu X J 2023 *Phys. Rev. Lett.* **131** 176401
[29] Jagannathan A 2021 *Rev. Mod. Phys.* **93** 045001
[30] Ostlund S, Pandit R, Rand D, Schellnhuber H J and Siggia E D 1983 *Phys. Rev. Lett.* **50** 1873
[31] Liu T and Xia X 2024 *Chin. Phys. Lett.* **41** 017102
[32] Tang L Z, Zhang G Q, Zhang L F and Zhang D W 2021 *Phys. Rev. A* **103** 033325
[33] Duncan C W 2024 *Phys. Rev. B* **109** 014210
[34] Yang C, Yang W Z, Wang Y J and Wang Y C 2024 *Phys. Rev. A* **110** 042205
[35] Wang Y C, Zhang L, Niu S, Yu D P and Liu X J 2020 *Phys. Rev. Lett.* **125** 073204
[36] Lin X S, Chen X M, Guo G C and Gong M 2023 *Phys. Rev. B* **108** 174206
[37] Zhang Y C and Zhang Y Y 2022 *Phys. Rev. B* **105** 174206
[38] Tong X Q, Zhang Y L, Li B and Yang X S 2025 arXiv:2501.14343
[39] Jiang X P, Zeng W L, Hu Y Y and Pan L 2024 arXiv:2409.03591
[40] Li S Z, Zhang Y C, Wang Y C, Zhang S C, Zhu S L and Li Z 2025 arXiv:2501.07866
[41] Kraus Y E, Lahini Y, Ringel Z, Verbin M and Zilberberg O 2012 *Phys. Rev. Lett.* **109** 106402
[42] Segev M, Silberberg Y and Christodoulides D N 2013 *Nat. Photonics* **7** 197
[43] Biddle J and Das Sarma S 2010 *Phys. Rev. Lett.* **104** 070601
[44] Ganeshan S, Pixley J H and Das Sarma S 2015 *Phys. Rev. Lett.* **114** 146601
[45] Wang Y C, Zhang L, Sun W, Poon T F J and Liu X J 2022 *Phys. Rev. B* **106** L140203
[46] Wang Y C, Zhang L, Wan Y H, He Y and Wang Y J 2023 *Phys. Rev. B* **107** L140201
[47] Lu Z P, Xu Z H and Zhang Y B 2022 *Ann. Phys. (Berlin)* **534** 2200203
[48] Xu Z H, Huangfu H L, Zhang Y B and Chen S 2020 *New J. Phys.* **22** 013036
[49] Xu Z H, Xia X and Chen S 2021 *Phys. Rev. B* **104** 224204
[50] Longhi S 2024 *Phys. Rev. Lett.* **132** 236301
[51] Liu T, Guo H, Pu Y and Longhi S 2020 *Phys. Rev. B* **102** 024205
[52] Liu T and Guo H 2018 *Phys. Rev. B* **98** 104201
[53] Longhi S 2024 *Phys. Rev. B* **110** 184201
[54] Maksymenko M, Honecker A, Moessner R, Richter J and Derzhko O 2012 *Phys. Rev. Lett.* **109** 096404
[55] Rhim J W and Yang B J 2021 *Adv. Phys.: X* **6** 1901606
[56] Wang Y F, Gu Z C, Gong C D and Sheng D N 2011 *Phys. Rev. Lett.* **107** 146803
[57] Danieli C, Bodyfelt J D and Flach S 2015 *Phys. Rev. B* **91** 235134
[58] Lee S, Andreanov A and Flach S 2023 *Phys. Rev. B* **107** 014204
[59] Liu H, Lu Z P, Xu X and Xu Z H 2024 *New J. Phys.* **26** 093007
[60] Kawabata K, Bessho T and Sato M 2019 *Phys. Rev. Lett.* **123** 066405
[61] Ding K, Zhang Z Q and Chan C T 2015 *Phys. Rev. B* **92** 235310
[62] Yao S Y and Wang Z 2018 *Phys. Rev. Lett.* **121** 086803
[63] Yao S Y, Song F and Wang Z 2018 *Phys. Rev. Lett.* **121** 136802
[64] Gong Z P, Ashida Y, Kawabata K, Takasan K, Higashikawa S and Ueda M 2018 *Phys. Rev. X* **8** 031079
[65] Cai Z T, Li H D and Chen W 2025 *Phys. Rev. Lett.* **134** 240201
[66] Li Y X, Li L H and Xu Z H 2025 arXiv:2508.02273
[67] Wang H M, Xu Z H and Li Z J 2025 *Phys. Rev. A* **112** 042230
[68] Longhi S 2019 *Phys. Rev. Lett.* **122** 237601
[69] Maimaiti W, Andreanov A, Park H C, Gendelman O and Flach S 2017 *Phys. Rev. B* **95** 115135
[70] Maimaiti W and Andreanov A 2021 *Phys. Rev. B* **104** 035115
[71] Wang Z H, Xu F M, Li L, Xu D H and Wang B 2022 *Phys. Rev. B* **105** 024514
[72] MacKinnon A and Kramer B 1983 *Z. Phys. B* **53** 1
[73] Liu Y X, Wang Y J, Zheng Z H and Chen S 2021 *Phys. Rev. B* **103** 134208
[74] Zeng Q B 2022 *Phys. Rev. B* **106** 235411
[75] Li X, Liu J and Liu T 2024 *Front. Phys.* **19** 33211
[76] Hofmann T, Helbig T, Lee C H, Greiter M and Thomale R 2019 *Phys. Rev. Lett.* **122** 247702
[77] Imhof S, Berger C, Bayer F, Brehm J, Molenkamp L W, Kiessling T, Schindler F, Lee C H, Greiter M, Neupert T and Thomale R 2018 *Nat. Phys.* **14** 925